Analysis of forced and intrinsic quenching in a plasma reactor for nitrogen fixation by use of three-dimensional simulations and experiments

Chemical Engineering Journal 543 (2026) 178575

Contents lists available at ScienceDirect

Chemical Engineering Journal

journal homepage: www.elsevier.com/locate/cej

Analysis of forced and intrinsic quenching in a plasma reactor for nitrogen fixation by use of three-dimensional simulations and experiments

Vikash Vashisth [a], Muzammil Iqbal [b], Thomas Butterworth [b], Gerard van Rooij [b], Ronnie Andersson [a,*]

[a] Department of Chemistry and Chemical Engineering, Chalmers University of Technology, SE-41296, Gothenburg, Sweden
[b] Faculty of Science and Engineering, Maastricht University, 6229 GS, Maastricht, the Netherlands

ARTICLE INFO

Keywords:
Nitrogen fixation
Plasma reactor
Forced quenching
Computational fluid dynamics
Chemical reaction engineering

ABSTRACT

Microwave plasma reactors offer a promising route for sustainable nitrogen fixation, yet the efficiency of NO_x production is often limited by fast backward reactions at elevated temperatures. This study employs three-dimensional CFD simulations, validated against experimental measurements, to investigate the impact of forced jet quenching on the thermo-fluid-chemical dynamics of NO_x formation. A split-feed configuration (10 SLM tangential plasma feed plus 10 SLM impinging quench jets) is compared with a conventional single-feed system relying solely on intrinsic quenching. The quench jets reorganize the flow, intensify local turbulence, and impose sharp thermal gradients that rapidly cool the plasma tail region where gas temperature falls from ~3500 K to below 800 K upon injection, suppressing NO_x destruction and stabilizing reaction products. Net reaction rates indicate that forced jet-quenching suppresses NO_x destruction and sustains higher yield across 400–800 W microwave power. These gains are achieved without an energy-efficiency trade-off, as evidenced by lower specific energy costs. Parametric analysis identifies the influence of jet location: positioning jets too near the plasma core leads to incomplete stabilization, while farther downstream offers negligible gains. Overall, forced jet quenching emerges as a robust, controllable complement that augments the reactor's intrinsic quenching to boost yield and energy efficiency. The validated modeling framework provides mechanistic insight and shows how to identify the configuration-specific upper bound in performance for a given reactor design.

1. Introduction

The advancement of sustainable nitrogen fixation (NF) technologies remains a critical research priority, driven by the escalating global demand for fertilizers required to sustain agricultural productivity amid rapid population growth. The Haber–Bosch (H—B) process, while historically transformative and still the most widely used industrial process for ammonia synthesis, is inherently energy-intensive (1–2% of global supply) and contributes substantially to global greenhouse gas emissions (around 300 million metric tons annually) due to its dependence on fossil-fuel-derived hydrogen and high operating pressures and temperatures [1,2]. Considering these environmental and energy concerns, considerable efforts have been directed toward developing alternative NF pathways that operate under milder conditions and offer improved sustainability metrics. Among these, plasma-assisted processes, biological nitrogen fixation, and metallocomplex-mediated mechanisms have garnered significant attention. Furthermore, a comprehensive comparative analysis of diverse NF strategies, evaluating their thermodynamic viability, scalability potential, and inherent technical constraints is essential for identifying feasible pathways toward sustainable and decentralized NF technologies [1]. Liu et al. [3] reviewed the fundamental reaction pathways governing nitrogen oxide (NO_x) formation, and their implications for energy efficiency in thermal and non-thermal environments, offering mechanistic insights essential for the rational design of next-generation NF systems. Plasma-assisted NF has gained increasing attention as a viable alternative to conventional thermochemical processes, particularly for decentralized and renewable-energy-driven production of nitrogen-based chemicals. Non-thermal plasmas can activate the strong N≡N bond under comparatively mild conditions, enabling the formation of nitrogen species such as nitric oxide (NO) and ammonia however, NO_x synthesis is often more favorable in warm plasma regimes. The use of air, an abundant, resilient and cost-effective feedstock, further enhances the attractiveness of plasma-based NF for sustainable applications [4]. Recent assessments of

* Corresponding author.
E-mail address: ronnie.andersson@chalmers.se (R. Andersson).

https://doi.org/10.1016/j.cej.2026.178575
Received 26 March 2026; Received in revised form 25 May 2026; Accepted 18 June 2026
Available online 19 June 2026

plasma NO_x synthesis indicate that warm plasmas generally provide higher NO_x yields and drop in energy costs than highly non-thermal plasmas, reflecting the strong temperature dependence of NO formation; this motivates the use of microwave plasma in the present work [5].

Over the years, researchers have studied a wide spectrum of plasma reactor configurations employed in experimental investigations, each offering distinct advantages in terms of discharge characteristics, energy efficiency, and scalability such as spark and glow [6,7], dielectric barrier discharge also known as highly non-equilibrium cold plasma [8], and gliding arc [9,10]. Significant experimental advancements have deepened the understanding of plasma-assisted nitrogen fixation and its broader applications. Recent progress of plasma-assisted NF research is reported by Li et al. [11]. In addition, microwave plasma (MW) reactors have been extensively utilized owing to their ability to generate high ionization fraction and facilitate efficient excitation of nitrogen molecules, thereby improving NO_x yield and overall energy efficiency [12–17]. Over the past few years, research into microwave plasma for NO_x formation has accelerated, yielding major insights into plasma-driven reaction mechanisms and process optimization. Typical range of operation conditions covers flow rates of 1–20 standard liters per minute (SLM), power input of 200–2000 W and sub- to atmospheric operating pressure range [12,18–21]. Most experiments rely on continuous-wave microwave operation, a choice that favours steady-state plasma conditions and facilitates direct measurement of process efficiency. Microwave plasma offers several intrinsic advantages that enhance its scalability and industrial relevance along with straightforward integration into existing infrastructures [12]. Recently, Shen et al. [15] demonstrated the use of microwave air plasma to boost the NO_x production by optimizing turbulence and maintaining non-thermal conditions. Helsloot et al. [16] utilized microwave plasma for the destruction of methane with the aim of converting methane into valuable agricultural products. This method presents a dual advantage: enabling the efficient production of nitrogenous agricultural inputs while concurrently mitigating enteric methane emissions, a major contributor to agricultural greenhouse gas emissions. Plasma technology is considered a novel approach for converting CO_2 into value-added chemicals and fuels [22]. Keifer et al. [23] employed a lab-scale microwave plasma torch for CO_2 dissociation and demonstrated that the microwave plasma can operate in a stable and reproducible manner. Rincón et al. [24] studied ethanol decomposition for hydrogen production using an argon microwave plasma and found efficient and clean hydrogen production at high gas temperature. Beyond chemical synthesis, MW systems have found extensive application in the field of biodecontamination and sterilization of bacteria and viruses [25–27].

A comprehensive understanding of the interactions among flow dynamics, temperature gradients, species transport, turbulence, electromagnetic energy coupling and the complex chemistry underlying plasma generation requires more than experimental observation alone. Because these processes occur over extremely short time scales and involve tightly coupled physical and chemical phenomena, direct experimental measurement is often limited. Consequently, computational fluid dynamics (CFD) have become a central tool for investigating plasma reactors. Such models make it possible to resolve the coupled transport and reaction mechanisms, evaluate the influence of operating conditions, and predict system behaviour under different flow conditions that are challenging to reproduce or measure experimentally. In recent years, increasingly sophisticated modeling approaches have been developed to capture the coupled plasma-chemical and flow phenomena in plasma reactors. For example, Marnef et al. [28] developed a 2–dimensional (2D) axisymmetric model for ammonia cracking in a warm arc plasma to solve 12 species and 23 reactions at different flow rates (5–20 SLM). Likewise, Wang et al. [10] proposed a 2D model of a gliding arc plasma reactor for CO_2 conversion, which they validated against experimental data under standard conditions of 2.5 SLM flow rate and 40 W power input.

Researchers have extensively used zero-dimensional (0D) and quasi-one-dimensional (quasi–1D) kinetic models to simulate plasma chemistry to manage the computational cost and complexity associated with simulating detailed plasma chemistry [29]. This approach substantially reduces the computational cost and the complexity associated with solving large reaction networks coupled with fluid dynamics. These simplified frameworks enable the incorporation of detailed reaction mechanisms, including vibrational and electronically excited species, but inherently lack three-dimensional resolution. Consequently, they fail to capture critical reactor characteristics such as temperature gradients, residence time distribution, and species transport, all of which significantly influence reactor performance and product selectivity. This emphasizes the need for three-dimensional (3D) simulations to accurately quantify the plasma reactor performance. Recently, Tatar et al. [30] developed a three-dimensional (3D) CFD framework to evaluate the performance of a microwave plasma reactor for direct NF, contributing to the understanding of intrinsic quenching mechanisms that suppress backward reactions and revealing complex three-dimensional flow and temperature distributions.

Plasma reactor performance can also be enhanced by introducing forced quenching using secondary gas injection [31,32] or quenching nozzles [33]. Perambadur et al. [31] modelled arc plasma reactor forced quenching using secondary gas co-current and counter-current injection without including chemical kinetics in the 3D simulations. The study primarily focused on bulk flow disturbances rather than plasma core behaviour, and the reaction chemistry was not included to isolate and evaluate the effect of forced quenching. Majeed et al. [32] also modelled an arc plasma forced quenching using 0D modeling and stated that both energy cost and system efficiency can be increased with thermal gas forced quenching. Van Alphen et al. [33] simulated the effect of quenching nozzles to improve the performance of CO_2 microwave plasma using a 3D CFD model and a quasi–1D kinetic model. Forced quenching has been shown to potentially improve plasma reactor performance; however, a fully coupled understanding that accounts for the complete interplay of flow dynamics and plasma chemistry inside a microwave plasma reactor is still lacking.

In this study, to the best of our knowledge, three-dimensional, transient, high-resolution turbulent simulations are performed for the first time to investigate the role of forced jet quenching on NO_x formation in a warm microwave plasma reactor (operating at 1 bar) incorporating non-equilibrium chemical reactions. The microwave discharge is treated as a warm, partially thermalized plasma, i.e. a plasma in which heavy species internal modes are in near equilibrium ($T_{rotational} \approx T_{vibrational}$) due to frequent collisions at 1 bar, while the electrons remain at a higher temperature. Consequently, the system is not in full local thermodynamic equilibrium (LTE), but exhibits partial local thermodynamic equilibrium (pLTE) for the heavy species. This pLTE assumption is supported by Raman spectroscopic data for atmospheric microwave plasmas and supports the use of a thermal chemistry model for heavy species kinetics [30]. With respect to the reaction kinetics, non-equilibrium refers to chemical non-equilibrium: reversible (forward and backward) reaction rates are finite, and species concentrations are not constrained to their chemical equilibrium values at the local temperature.

While the N_2–O_2 mixture is tangentially injected through the main inlet in the baseline case, forced quenching is introduced via two opposing central jets that deliver an additional N_2–O_2 stream directly after the plasma reaction zone. This unique configuration enables a direct comparison between passive (intrinsic) and active (forced) quenching mechanisms and their impact on flow dynamics, thermal fields, and species distribution governing NO_x formation. Transient large-eddy simulations (LES) coupled with a five-species kinetic model are used to analyze turbulence–chemistry interactions in the reactor at high Reynolds numbers, and the governing equations are solved using the CFD software ANSYS Fluent on a high-performance computing (HPC) cluster. Compared to the corresponding steady-state simulations,

the transient LES required at least 100 times more computational resources (core-hours). Furthermore, the simulations are quantitatively validated against Fourier-transform infrared (FTIR) spectroscopy measurements, ensuring consistency between predicted and observed NO_x mole fraction under varying flow and power conditions. This combined CFD–experimental approach offers new understanding of the coupled effects of turbulence, thermal transport, and plasma-driven chemistry, and demonstrates that forced jet quenching is an effective strategy for enhancing the yield of NO_x in plasma-based nitrogen fixation.

2. Experimental methodology

The experimental setup features a microwave-driven plasma reactor equipped with integrated jet quenching. The reactor consists of a quartz glass tube with an internal diameter of 26 mm, which is mounted inside a WR340 waveguide and energized by a solid-state microwave generator operating at 2.45 GHz with output power of 3 kW. For the present study, the reactor was operated at plasma power levels ranging from 400 to 700 W at 1 bar pressure. The working fluid was dried, compressed air supplied at a total flow rate of 20 (SLM). This flow was divided into two equal streams (10 SLM each): one introduced tangentially as the primary inlet to sustain the plasma core, and the other injected perpendicularly through two impinging quenching jets directed toward the reactor centreline. In this configuration, the quenching jets converge and impinge directly after the plasma region rather than entering tangentially, aiming to produce an intense localized cooling effect that rapidly drops the temperature and inhibits loss of nitrogen oxides by preventing backward reactions. This arrangement not only enables rapid thermal quenching of reactive species, suppressing back-reactions, but also enhances mixing and provides additional control over residence time and product yield. Cold air jets were used here to isolate the quenching effect without introducing additional reactive species. Other quenching media, such as water vapor or liquid droplets, could in principle enhance the cooling rate through higher heat capacity or latent heat effects; however, they will also modify the plasma chemistry via additional reactive radicals (e.g., OH and H) associated with water injection.

To quantify the gas-phase products, the NO_x mole fraction downstream of the reactor was continuously measured using a Bruker Invenio R Fourier Transform Infrared (FTIR) spectrometer equipped with an MCT detector. The FTIR gas cell was maintained at 0.2 bar, a pressure low enough to minimize spectral line broadening and prevent condensation of dinitrogen tetroxide (N_2O_4). This combination of microwave power delivery, vortex-stabilized flow, centralized jet-assisted quenching, and FTIR diagnostics enables a detailed characterization of the plasma's chemical performance under controlled operating conditions. A similar system with in-situ laser scattering diagnostics was documented in our previous work [30] for single-feed system limited to 0.65 bar operating pressure. Experimental findings in our previous work demonstrated no significant influence of vibrational excitation (measured at multiple locations within the reactor), and no difference between vibrational and rotational temperatures was observed at this condition. Since the operating pressure in the present study does not differ significantly from those conditions, direct temperature measurements were not performed. Instead, the temperature profiles numerically and experimentally reported at 0.65 bar are used as a benchmark and later compared with the CFD predictions at 1 bar presented in this paper to assess the impact of operating pressure on thermal behaviour. The schematic layout of the experimental setup used in this study is illustrated in Fig. 1.

3. Numerical modeling methodology and validation

3.1. Governing equations

The jet flow attains high Reynolds numbers due to high-velocity injection through the quench inlets, thereby inducing turbulence in the jets mixing region. In such flows, inertial forces dominate over viscous forces, leading to chaotic and fluctuating motion. The governing equations for the large eddy simulations (LES) are expressed in terms of the filtered instantaneous velocity field ($\vec{u}$). The continuity equation for the mixture, enforcing mass conservation, is expressed as in Eq. (1)

$$\frac{\partial \rho}{\partial t} + \nabla \cdot (\rho \vec{u}) = 0 \tag{1}$$

The conservation of each chemical species within the reactor is described by the corresponding species transport equation, which accounts for convection, effective diffusion ($\vec{J}_{i,\ eff}$), and source terms (S_i) due to chemical reactions. This is expressed in Eq. (2)

$$\frac{\partial (\rho m_i)}{\partial t} + \nabla \cdot (\rho \vec{u} m_i) + \nabla \cdot \vec{J}_{i,eff} = S_i \tag{2}$$

The momentum conservation is governed by the filtered Navier–-Stokes equation in the context of large eddy simulation (LES) and expressed in Eq. (3)

$$\frac{\partial (\rho \vec{u})}{\partial t} + \nabla \cdot (\rho \vec{u} \vec{u}) = -\nabla p + \nabla \cdot \left[(\nu_{eff}) \nabla \vec{u} \right] \tag{3}$$

where ν_{eff} represents the effective kinematic viscosity introduced in LES to account for unresolved turbulent motion. p and ρ represent pressure and density of the fluid, respectively.

The total energy of a fluid element is governed by the energy conservation equation, Eq. (4)

$$\frac{\partial (\rho E)}{\partial t} + \nabla \cdot (\vec{u}(\rho E + p)) = \nabla \cdot \left[\lambda_{eff} \nabla T - \sum_i h_i \vec{J}_{i,eff} + (\bar{\tau} \cdot \vec{u}) \right] \tag{4}$$

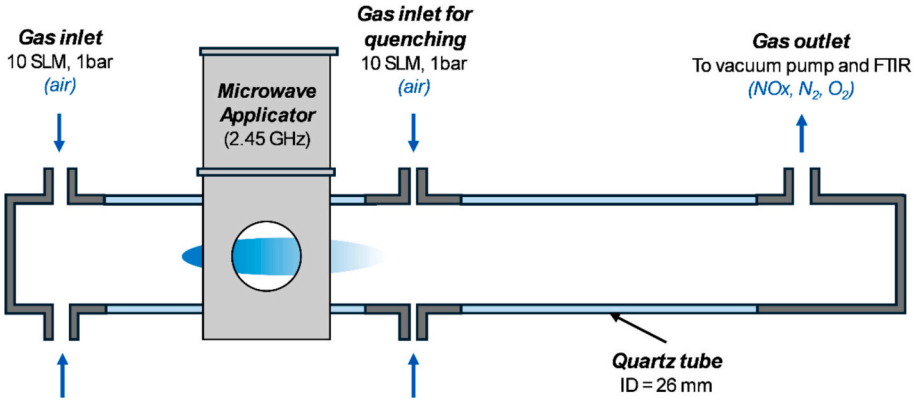

Fig. 1. Schematic layout of the experimental setup with primary gas inlet and secondary inlet for forced jet quenching aligned with FTIR measurement.

where E represents the sum of enthalpy, static energy and kinetic energy of a fluid element and h_j is the sensible enthalpy of species, $\bar{\tau}$ is the tensor of shear stress, λ_{eff} is effective thermal conductivity, and T is temperature.

3.2. Chemical non-equilibrium reaction modeling

To compute the source term in Eq. (2) for each chemical species, a finite-rate model was employed for turbulence-chemistry interaction. In the high temperature NO formation environment, reaction rates are predominantly governed by chemical kinetics rather than by turbulent mixing as N_2 and O_2 are premixed. Reaction rates were calculated using Arrhenius expressions, while the chemical reactions were treated as non-equilibrium and reversible. With respect to the chemical reactions, non-equilibrium refers to chemical non-equilibrium: reversible (forward and backward) reaction rates are finite, so species concentrations are free to deviate from their chemical equilibrium values at the local temperature. The forward rate constant for each reaction was determined according to the Arrhenius formulation presented in Eq. (5)

$$k_{f,r} = A_r T^{\beta_r} exp\left[-\left({}^{E_r}/_{RT} \right) \right] \tag{5}$$

where R denotes the universal gas constant, A_r is the pre-exponential factor, β_r is temperature exponent, and E_r is activation energy. The backward rate constant for the reaction is computed using the relation given in Eq. (6)

$$k_{b,r} = \frac{k_{f,r}}{K_r} \tag{6}$$

The equilibrium constant K_r for each reaction is calculated as a function of the Gibbs free energy. Consequently, chemistry is treated in chemical non-equilibrium: species concentrations are not constrained to their chemical equilibrium values at the local temperature, chemical equilibrium is recovered only as a limiting case at long times. In this study, the chemical kinetics of the system were modelled using a five-species model (N_2, O_2, NO, N, O) proposed by Park [34], as summarized in Table 1. Here, M_{mol} refers to the molecular species (N_2, O_2, and NO), while M_{atom} denotes the atomic species (N and O). In Table 1, the first three reactions are written in contracted third-body form, where each line represents five distinct reactions corresponding to the five possible collision partners (M = N_2, O_2, NO, N, O). These three lines therefore correspond to reactions 1–5, 6–10, and 11–15, respectively. The final two lines are binary reactions and correspond to reactions 16 and 17. Among the full set, seven reactions involve NO directly.

Table 1
Chemical reaction mechanisms and kinetic parameters used in the CFD simulations.

Expanded reaction numbering	Reactions	$A_r\left(\frac{cm^3}{mole.s}\right)$	β	E_r/R
R 1–5	$N_2 + M \leftrightarrow N + N + M$	$M = M_{mol}$: 7.0×10^{21}	−1.6	113200
		$M = M_{atom}$: 3.0×10^{22}	−1.6	
R 6–10	$O_2 + M \leftrightarrow O + O + M$	$M = M_{mol}$: 2.0×10^{21}	−1.5	59500
		$M = M_{atom}$: 1.0×10^{22}	−1.5	
R 11–15	$NO + M \leftrightarrow N + O + M$	$M = M_{mol}$: 5.0×10^{15}	0.0	75500
		$M = M_{atom}$: 1.1×10^{17}	0.0	
R 16	$N_2 + O \leftrightarrow NO + N$	6.4×10^{17}	−1.0	38400
R 17	$NO + O \leftrightarrow O_2 + N$	8.4×10^{12}	0.0	19450

The vibrational and rotational temperatures were known to be equal at 0.65 bar and 20 SLM [30]. In the present study at 1 bar, the faster vibrational relaxation further reduces the difference between vibrational and rotational temperatures, thereby validating the application of this kinetic scheme for accurately describing the reactive processes under the conditions studied.

3.3. Transport properties and thermodynamic model

The kinetic gas theory is used to compute the individual species transport properties (fluid viscosity and thermal conductivity) as given in Eq. (7) and Eq. (8), respectively

$$\mu_i = 2.67 \times 10^{-6} \frac{\sqrt{M_i T}}{\sigma_i^2 \Omega_{\mu i}} \tag{7}$$

$$\lambda_i = \frac{15}{4} \frac{R}{M_i} \mu_i \left[\frac{4}{15} \frac{C_{pi} M_i}{R} + \frac{1}{3} \right] \tag{8}$$

where M_i represents the molar mass of species i, and σ_i and $\Omega_{\mu i}$ denote the corresponding Lennard–Jones parameter and collision integral for diffusion, respectively. μ_i and C_{pi} denote dynamic viscosity and specific heat capacity.

The mixing law is used to compute the mixture viscosity as given in Eq. (9)

$$\mu = \sum_i \frac{X_i \mu_i}{\sum_j X_j \phi_{ij}} \tag{9}$$

where X_i is the mole fraction of species i and the function ϕ_{ij} is given by Eq. (10):

$$\phi_{ij} = \frac{\left[1 + \left(\frac{\mu_i}{\mu_j} \right)^{0.5} \left(\frac{M_{w,j}}{M_{w,i}} \right)^{0.25} \right]^2}{\left[8 \left(1 + \frac{M_{w,i}}{M_{w,j}} \right) \right]^{0.5}}. \tag{10}$$

The mixing law was also used for the thermal conductivity of the mixture and given by Eq. (11):

$$\lambda = \sum_i \frac{X_i \lambda_i}{\sum_j X_j \phi_{ij}}. \tag{11}$$

Furthermore, kinetic gas theory is used for the computation of mass diffusivity and thermal diffusion coefficient of the mixture.

The reactor is treated as a warm plasma, meaning that the model assumes thermal equilibrium among heavy-particle internal modes while still treating the reacting mixture in chemical non-equilibrium. As reported by Tatar et al. [30], Raman spectroscopy measurements show that vibrational–rotational non-equilibrium is negligible at this operating condition. A similar observation was made by Van de Steeg et al. [35] using a setup similar to the one in the present study, regarding vibrational relaxation times for N_2, CH_4 and CO_2. The specific heat of each species is considered as a function of temperature and nasa-9-piecewise-polynomial equations are used to evaluate the specific heat. The specific heat of the gas mixture was evaluated using a mass-fraction-weighted averaging approach, expressed in Eq. (12)

$$C_p = \sum_i W_i C_{pi}. \tag{12}$$

where, W_i is mass fraction of species i.

3.4. Boundary condition and numerical scheme

The thermal boundary condition at the reactor wall was specified to account for both local external convective and local radiative heat

losses. Under steady-state operating conditions, these losses are balanced by the heat flux traversing the reactor wall locally, resulting in a spatially varying wall temperature. The external local free-convection heat transfer coefficient was determined using the Nusselt number correlation, while the local radiative heat loss was calculated based on the local outer wall temperature [36].

Specification of the wall thickness, thermal conductivity, and external surface emissivity closed the boundary conditions, enabling evaluation of heat losses at all external boundary nodes. The shape and size of the microwave heat source were inferred from auto-exposed plasma discharge images, following established image-based analyses of microwave plasma coupling regions [30]. This approach was adopted because it is not computationally feasible to resolve the fully coupled three-dimensional turbulent flow and electromagnetic field equations within the present modeling framework. The shape and size of the microwave heat source were similar at 1 bar and 0.65 bar; therefore, a similar heat source region with radius 2.4 mm was used in the present study. The heat-source geometry and power-deposition profile were kept identical for all cases (forced jet-quenching and non-quenched) to isolate the effect of quenching-driven flow and mixing and defined so that the volume-integrated heat source equals the imposed power input for the respective operating condition. This ensures that performance differences are attributable solely to quenching-induced transport effects. To produce a cigar-like shape the cylindrical heating-source region was modified by rounding the end sections, while the radius of the central region was kept constant at 2.4 mm.

No slip wall boundary condition was used for reactor walls. Bounded central differencing was used for spatial discretization, while implicit time integration was employed. Both first-order and second-order implicit time-integration schemes were examined in a time-step sensitivity study to assess numerical stability and temporal accuracy in the presence of stiff chemistry. Transient large eddy simulations (LES) were conducted to resolve the complex flow field and quantify the effects of intense turbulence induced by jet quenching, employing the dynamic Smagorinsky–Lilly subgrid-scale model. As emphasized by Pope [37], the dynamic Smagorinsky–Lilly formulation is particularly well-suited for flows that transition between laminar and turbulent regimes, since it adapts the subgrid viscosity locally based on the resolved scales and resolve the dynamics around the wall. By accounting for local flow anisotropy and varying shear conditions, the dynamic model provides a more physically consistent representation of turbulent transport, making it especially appropriate for plasma reactors where sharp gradients, strong shear layers, and laminar-turbulent coexistence are simultaneously present. As illustrated in Fig. 2, the flow within the bulk of the reactor remains predominantly laminar whereas the region surrounding the jet injection (denoted by dashed line at x/D = 8.08) exhibits markedly elevated turbulence levels due to strong mixing. The turbulence intensity reaches a maximum in the vicinity of the quenching jets and progressively diminishes downstream. A density based coupled solver was employed to resolve the strong interactions among the flow, temperature, and species transport fields.

3.5. Mesh and time independence

The reactor domain was discretized on a high-quality mesh tailored for LES, to capture the strong turbulence induced by jet quenching. The mesh provides adequate resolution of both near-wall region and bulk flow structures. Confidence is gained that the present mesh resolution is sufficient to resolve the key flow, thermal, and chemical species of the plasma. Mesh resolution and time-step size were systematically assessed through grid and time sensitivity analysis to guarantee numerical stability and physical accuracy. The criterion for model resolution was based on the ratio of resolved turbulent kinetic energy (TKE) to the total TKE. In the present simulations, approximately 94% of the TKE was directly resolved (Mesh 1), substantially surpassing the commonly accepted threshold of 80% recommended in the literature [38,39].

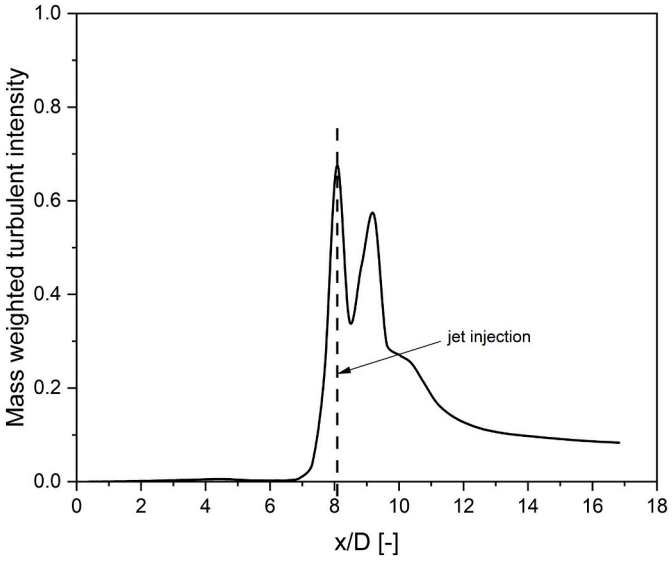

Fig. 2. Mass-weighted average turbulent intensity in the reactor at different axial locations.

Further, mesh refinement adaptation was applied in regions of high turbulence to validate mesh independence and approximately 96% of the TKE was resolved (Mesh 2). The volume integral of the net NO formation rate in the reactor [kmol/s] was also monitored across successive mesh refinements for consistency and summarized in Table 2. Mesh independence was achieved at approximately 8.4 million cells. In addition, time-step independence was evaluated, with the results summarized in Table 3. Together with the grid-independence analysis, these results indicates that numerical diffusion does not significantly influence the predicted nitrogen fixation within the reactor at the employed spatial and temporal resolution. This high level of resolution confirms that the large eddy simulations capture the dominant flow structures and turbulent energy-containing scales, thereby providing high-fidelity predictions of the coupled fluid dynamic–thermal–chemical processes within the plasma reactor. The computational data in this study was benchmarked against the numerical and experimental data reported in our previous work [30] showing consistency. Specifically, temperature profiles along both the axial and radial directions were analysed for the reference case of 20 SLM total flow at 1 bar operating pressure without jet quenching and compared with the profiles obtained at 20 SLM and 0.65 bar. As shown in Fig. 3, the comparison demonstrates excellent overall agreement, confirming the reliability of the present model across different pressure conditions. Detailed inspection of the temperature fields reveals overall minor differences between the two operating pressures, primarily localized to the plasma core region. At 1 bar, the plasma core temperature is marginally lower (at y = 0 mm) than at 0.65 bar, whereas temperatures farther from the core (at y = 6 mm) are slightly higher. Although the available temperature measurements were obtained at a slightly lower pressure (0.65 bar), they provide valuable support for assessing model accuracy, particularly since the simulations explicitly resolve the temperature field at 1 bar and only minor differences are expected between these pressures. At the higher pressure of 1 bar, vibrational relaxation times are even shorter, further supporting the assumption that heavy-species internal modes remain close to

Table 2
Summary of the mesh-independence analysis for jet quenching.

	Mesh 1	Mesh 2
Cells [number]	8.4 million	10.8 million
Resolved TKE [%]	94%	96%
Volume integral NO formation rate [kmol/s]	1.25e-07	1.25e-07

Table 3
Summary of the time-independence analysis for jet quenching.

	Volume integral NO formation rate [kmol/s] Time step size 1e-04 [s]	Volume integral NO formation rate [kmol/s] Time step size 1e-05 [s]	Volume integral NO formation rate [kmol/s] Time step size 1e-06 [s]
Bounded Central Differencing + First Order Implicit	1.26e-07	1.25e-07	1.25e-07
Bounded Central Differencing + Second Order Implicit	1.26e-07	1.25e-07	1.25e-07

equilibrium under the present conditions. In addition, chemical validation is provided by FTIR measurements of NO_x production performed in the same reactor at 1 bar over the identical input-power range as the simulations, offering direct validation of nitrogen fixation under matching operating conditions as presented in the Results and Discussion section.

Furthermore, the close agreement between the present study and mesh independent reference data highlights the adequacy of the mesh resolution employed in this study. The combination of fine meshing in regions of steep gradients with good resolution in the bulk flow yielded grid-independent results. This benchmarking confirms that the present CFD framework can accurately capture the interplay between flow, temperature, and plasma chemistry under varying operating conditions.

4. Results and discussion

4.1. Analysis and validation of flow, thermal and species transport

The impact of impinging jet injections for quenching on the internal flow dynamics of the plasma reactor is investigated. In this configuration, 10 SLM of gas is introduced through the main tangential inlet, while an additional 10 SLM is supplied via the dedicated quenching jets. As illustrated in Fig. 4, the introduction of the quenching streams fundamentally alters the hydrodynamic structure along the reactor axis. Fig. 4a illustrates representative flow profiles at multiple axial positions within the reactor. Different velocity scales are used for better visualization of the velocity profiles at each location. In the main inlet region, a weak reverse flow is observed (Line 1), followed by the formation of a stagnation point (Line 2). Notably, the intense turbulence generated near the quenching jets induces localized backflow (as shown on Lines 3 and 4), which gradually weakens downstream as the jet momentum dissipates and gas expansion aligns with the bulk flow direction. Near the quenching jets, the flow exhibits strong recirculation and back-and-forth motion driven by intense turbulence and momentum exchange between the core and injected streams. Downstream of the jet interaction zone, defined as the region from one tube diameter upstream to two tube diameters downstream, the flow accelerates and gradually relaxes into a more developed flow profile characteristic of tubular reactors (Line 5). In the upstream portion of the reactor, the gas retains a residual swirling pattern induced by the tangential inlets. This swirl interacts synergistically with the incoming quenching jets, improving mixing and enhancing momentum redistribution across the reactor cross-section. Fig. 4b illustrates this interaction with streamlines, demonstrating how the combined effect of swirl and jet quenching generates a complex flow structure conducive to rapid quenching and efficient species transport.

Fig. 5 illustrates the instantaneous distribution of temperature inside the reactor in a cross-sectional plane at power input of 400 W. The contours reveal a pronounced radial temperature gradient, with steep gradients occurring between the hot plasma core and the surrounding colder regions. In contrast, the plasma core itself exhibits a relatively uniform temperature field, reaching peak temperature close to 5970 K. The extremely high thermal environment drives strong dissociation of molecular species. Downstream of the plasma zone, the gas temperature is approximately 3500 K prior to jet injection. Following the introduction of the quenching jets, however, the temperature drops dramatically

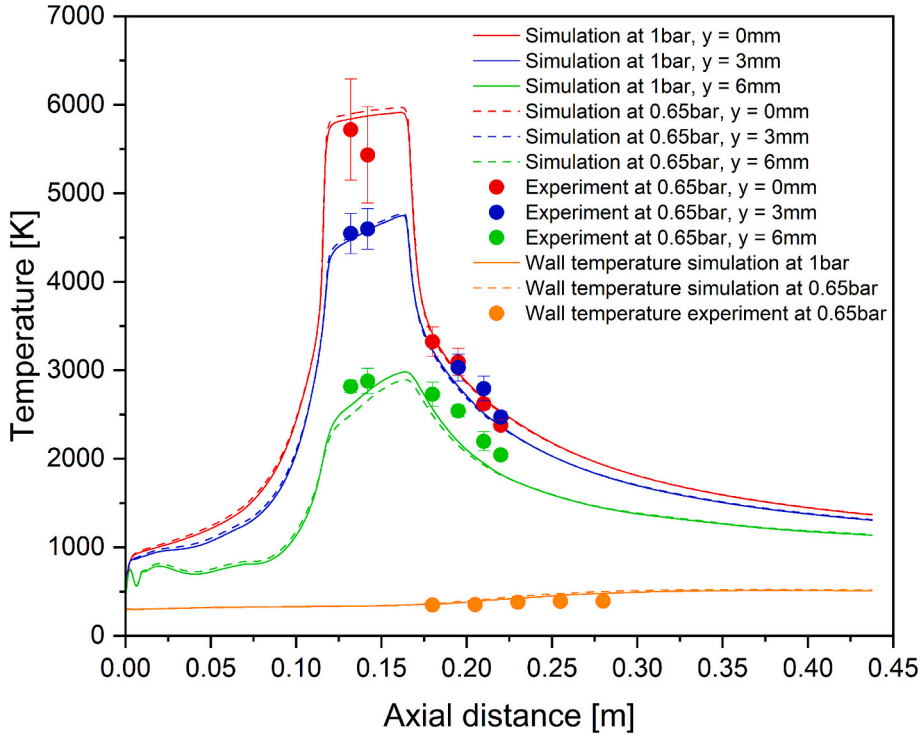

Fig. 3. Validation of gas temperatures inside the reactor and wall temperatures for a standard case at 20 SLM flow rate.

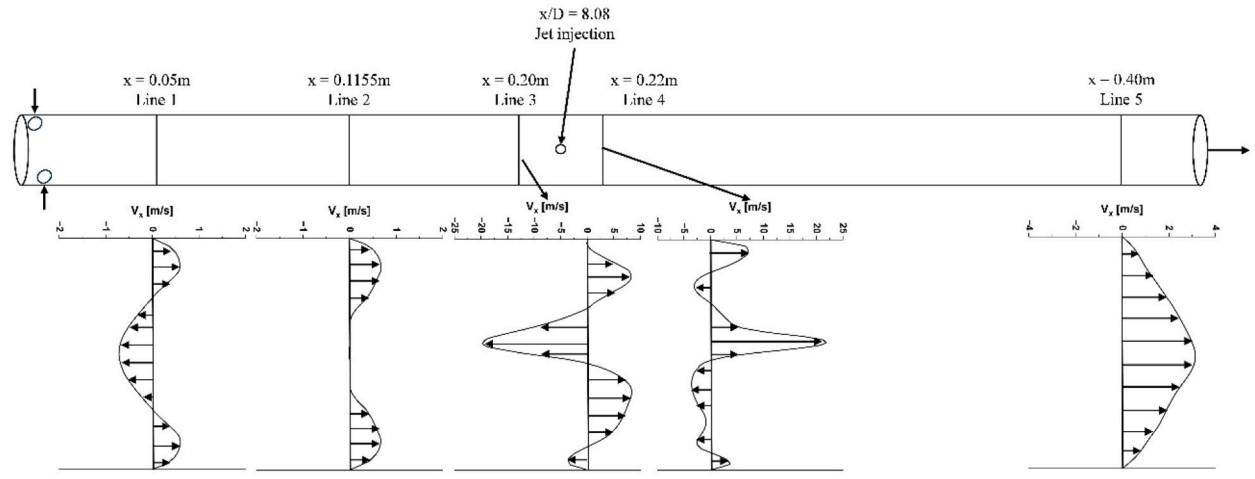

a.)

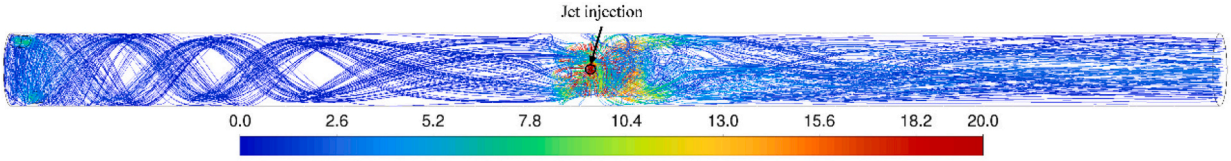

b.)

Fig. 4. a.) Mean x–velocity component at five different cross-sectional locations in the reactor; b.) Streamlines coloured by velocity magnitude. Both figures use the unit [m/s].

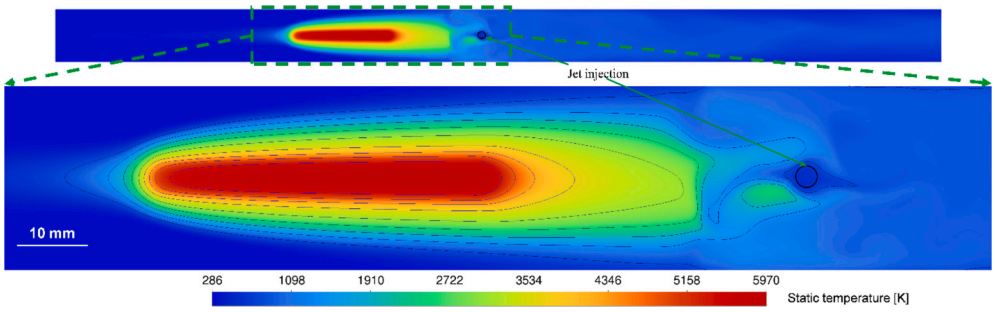

Fig. 5. Instantaneous temperature distribution in a cross-sectional plane in the middle of the reactor at power input of 400 W.

to about 800 K. This clearly demonstrates the effectiveness of the jet quenching strategy in rapidly cooling the hot gas and suppressing backward reactions. The reactor wall temperature is higher near the jet injection area but declines sharply downstream following the quenching action of the jets. The introduction of the jets intensifies the axial and radial temperature gradients, thereby promoting rapid thermal quenching.

The temperature distribution inside the reactor exerts a dominant influence on the formation, transport, and stabilization of chemical species. The simulations indicate that the dynamics inside the reactor

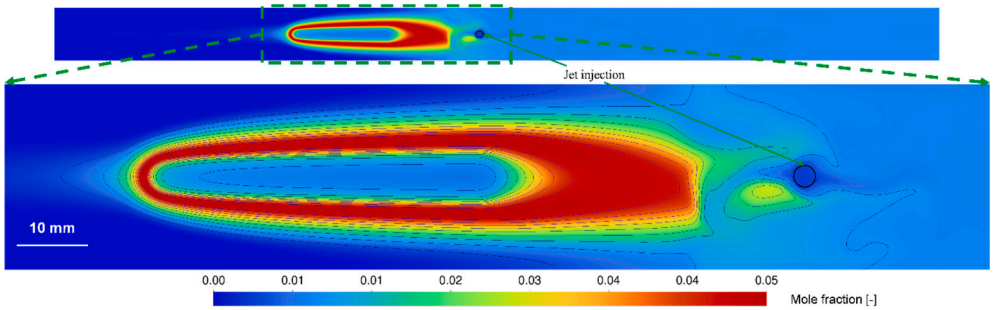

Fig. 6. Instantaneous NO mole fraction distribution in a cross-sectional plane in the middle of the reactor at power input of 400 W.

are highly heterogeneous, containing zones where forward reactions dominate and adjacent regions where backward reactions prevail. This dynamic interplay leads to pronounced variations in the molar fraction of species across the reactor volume. Fig. 6 presents the instantaneous distribution of NO mole fraction following forced jet quenching at power input of 400 W. The results clearly show that the injected quenching jets penetrate deeply into the reaction zone, disrupting equilibrium conditions and suppressing backward reactions. This intervention stabilizes NO production and sustains higher mole fractions toward the reactor outlet. Within the microwave plasma core (where the temperature is close to 5970 K), a local minimum in NO mole fraction is observed, which is attributed to the thermally induced instability of the NO bond at such high temperatures. The model predicts a maximum NO mole fraction of 4.97% at 3500 K, 1 bar, which compares favourably with the equilibrium estimate from Gibbs free energy calculations of 5.24% at 1 bar operating pressure. At 5970 K, the predicted NO mole fraction decreases to 0.80%, again closely matching the Gibbs free energy prediction of 0.83%. These values provide a valuable sanity check of the kinetic model, particularly in regions where the temperature is sufficiently high that the reaction time constants are smaller than the local cell residence time, leading to kinetic model predictions that are locally consistent with thermodynamic constraints.

Overall correspondence between simulation results and thermodynamic equilibrium calculations supports both the chemical kinetics implementation and the transport modeling in the present CFD framework. It also highlights the model's capability to accurately resolve the coupled effects of flow, heat transfer, and plasma chemistry governing NO formation and depletion within the reactor under the investigated operating conditions. A comparison of the instantaneous temperature (Fig. S1) and NO mole-fraction (Fig. S2) distribution in the reactor cross-section at 400 W for the forced jet-quenched and non jet-quenched systems is provided in the Supplementary data.

The overall NO production at the reactor outlet is quantified using a mass flow-weighted average, which incorporates the local mole fraction (y), gas density (ρ), and velocity field distribution ($\vec{u}$), at the reactor outlet, expressed in Eq. (13). This allows direct validation between the simulated and the FTIR measurements.

$$\bar{y} = \frac{\iint y\rho(\boldsymbol{u}\cdot\boldsymbol{n})dA}{\iint \rho(\boldsymbol{u}\cdot\boldsymbol{n})dA} \tag{13}$$

Validation and comparison of CFD predictions with experimental measurements of NO_x mole fraction at the reactor outlet under different flow configurations (20 SLM single inlet vs. 10 + 10 SLM with jet quenching) and plasma power inputs ranging from 400 to 700 W are presented in Fig. 7. The CFD model successfully captures the overall NO_x formation trends and shows close agreement with the experimental data across the investigated operating conditions. Both the simulations and experiments reveal an essentially linear increase in NO_x mole fraction with increasing microwave power, irrespective of the flow configuration. However, the introduction of jet quenching consistently enhances NO_x formation compared to the non-quenched configuration at equivalent power levels. This enhancement is attributed to rapid cooling that stabilizes the system and suppresses backward reactions and prevents NO loss.

In addition, the energy cost analysis shown in Fig. 8 demonstrates that the jet-quenched configuration exhibits a measurably lower specific energy consumption compared to the non-quenched system, thereby enhancing the overall process efficiency. The energy cost is defined as the input power per amount of fixed nitrogen (on a mol-N basis). Experimentally, the specific energy consumption decreased by approximately 14–17% for the quenched configuration relative to the non-quenched case, while the CFD simulations predicted a corresponding reduction of 6–8%. This difference may be attributed to the plasma being represented by a homogeneous volumetric heat source, as well as to the kinetic mechanism employed in the simulations, which may under-represent the sensitivity of NO retention to rapid post-plasma cooling. Despite this difference, both experiments and simulations show consistent trends and comparable percentage-level improvements, confirming that forced quenching reduces the energy cost. The correlation between simulated and measured energy costs further supports the predictive capability of the CFD framework in capturing the coupled thermo-fluid–chemical dynamics governing NO_x formation in microwave plasma reactors. In the jet-quenched configuration, increasing microwave power increases the gas temperature and reaction rates in the hot zone, but the quenching jet limits the extent of post-formation backward reactions and drives the system toward a regime where NO production increases approximately proportionally with power over the investigated range. As a result, the energy cost shows only a weak dependence on power and appears nearly constant over the investigated range (Fig. 8) In contrast, in the non-quenched case, higher power more strongly increases the residence time at elevated temperature and enhances destruction pathways by radical recombination (reverse Zeldovich) reactions, so the NO production does not scale as favourably with power, yielding a more pronounced energy cost increase.

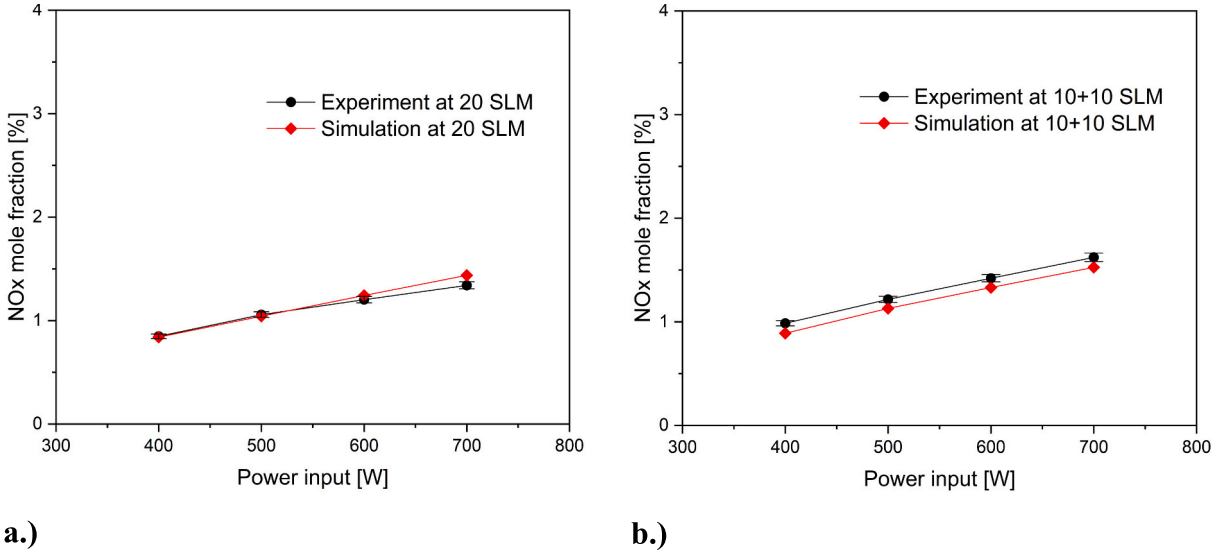

Fig. 7. Comparison between experimental and simulated NO_x mole fraction at the reactor outlet as a function of power input a.) intrinsically quenched reactor, b.) forced jet quenched reactor.

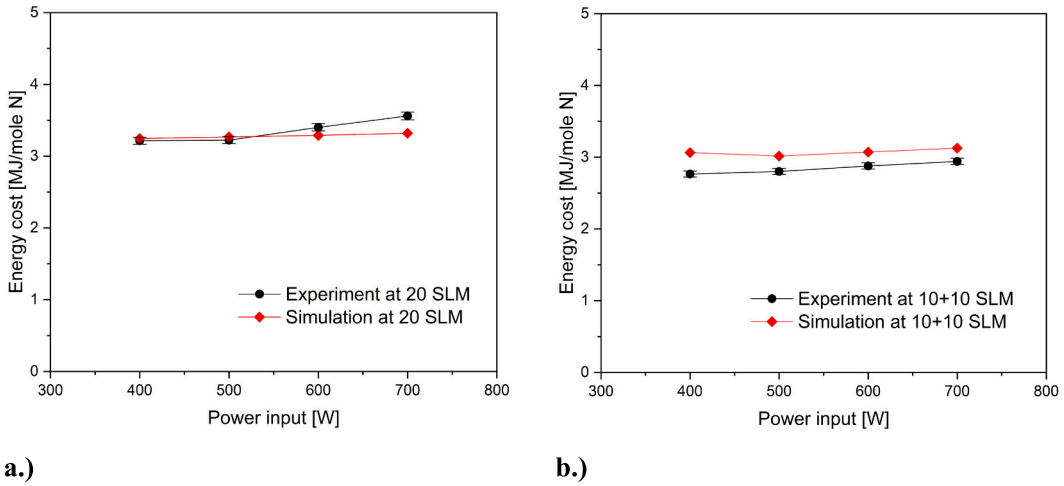

Fig. 8. Comparison between experimental and simulated energy cost of the nitrogen fixation as a function of power input a.) intrinsically quenched reactor, b.) forced jet quenched reactor.

4.2. Analysis of chemical reactions and forced jet quenching

Nitrogen fixation in the plasma reactor is initiated at high temperatures. Fig. 9 illustrates the nitrogen fixation zone, observed as an ellipsoidal high-temperature region at the plasma core, along with the spatial distribution of the net NO formation rate in a cross-sectional plane in the reactor. The simulation results highlight the coexistence of both forward and backward reactions throughout the plasma zone. At such temperatures, NO is continuously produced via forward reactions involving atomic oxygen and nitrogen molecules but simultaneously destroyed through radical mediated backward pathways and thermal dissociation pathways. A high rate of NO formation is concentrated in the hollow region around the plasma core and as the flow progresses downstream, the net production rate decreases, and destruction increases. The introduction of jet quenching rapidly reduces the local temperature, which strongly suppresses the backward reactions (as evidenced in the enlarged view of Fig. 9). This stabilizes NO production and increases the overall yield at the outlet.

The contour maps further reveal that the hollow red region encircling the plasma core corresponds to domains dominated by backward reactions (net NO destruction dominates), primarily the thermal dissociation of NO at high temperatures. In contrast, the blue regions denote zones favorable for net NO production, where lower temperatures and rapid quenching inhibit decomposition pathways. Within the chemical kinetic framework employed in this study, a total of 17 reversible elementary reactions were considered to capture the dominant plasma-assisted air chemistry pathways. Among these, seven reactions explicitly involve NO either as a reactant or a product, thereby governing the key routes of NO formation and depletion. In particular, the Zeldovich reactions emerge as the principal thermal reactions responsible for NO generation under high-temperature non-equilibrium conditions. Rapid thermal quenching downstream significantly alters the reaction rates and balance of the reactions and the abrupt decrease in temperature inhibits the reverse reactions responsible for NO dissociation, effectively suppressing NO destruction. This analysis demonstrates that the interplay between local temperature gradients, flow dynamics, and chemical kinetics critically determines the distribution of NO within the reactor. To better distinguish the domains of net NO formation and destruction, the simulation results are decomposed into positive and negative contributions to the net reaction rate. Fig. 10a highlights the regions of net NO formation, whereas Fig. 10b isolates the regions dominated by NO destruction. This separation provides a clearer visualization of the competing reaction pathways within the reactor and allows direct identification of zones where forward and backward reactions prevail under the coupled influence of temperature gradients and flow dynamics. The instantaneous temperature and NO mole-fraction distributions in the same cross-sectional planes are shown in Figs. 5 and 6, respectively.

The simulations reveal that intrinsic quenching, driven by the steep radial temperature gradients in the plasma core, effectively preserves NO along the radial direction. Beyond this, a significant portion of NO is maintained in the downstream direction through forced jet quenching, which generates sharp axial temperature gradients that rapidly cool the gas and suppress thermal decomposition. Fig. 11 illustrates the effect of forced jet quenching on a representative cross-sectional plane, superimposed with isocontours of the net rate of NO destruction. The negative isocontours indicate regions dominated by NO destruction. In the absence of forced quenching, these regions are more extensive, with

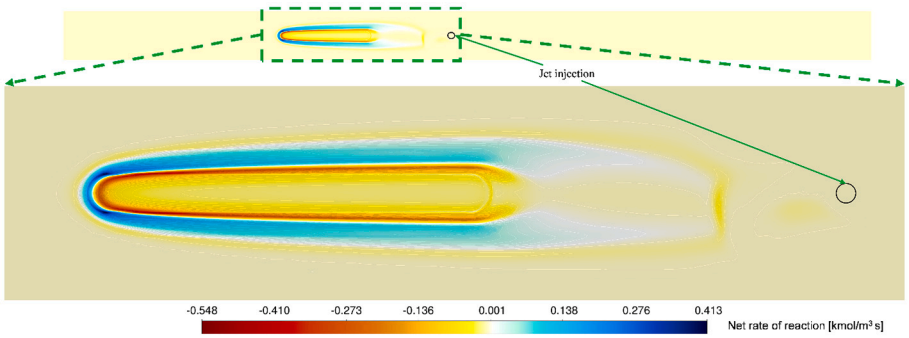

Fig. 9. Net NO formation rate distribution in a cross-sectional plane in the middle of the reactor during forced jet quenching.

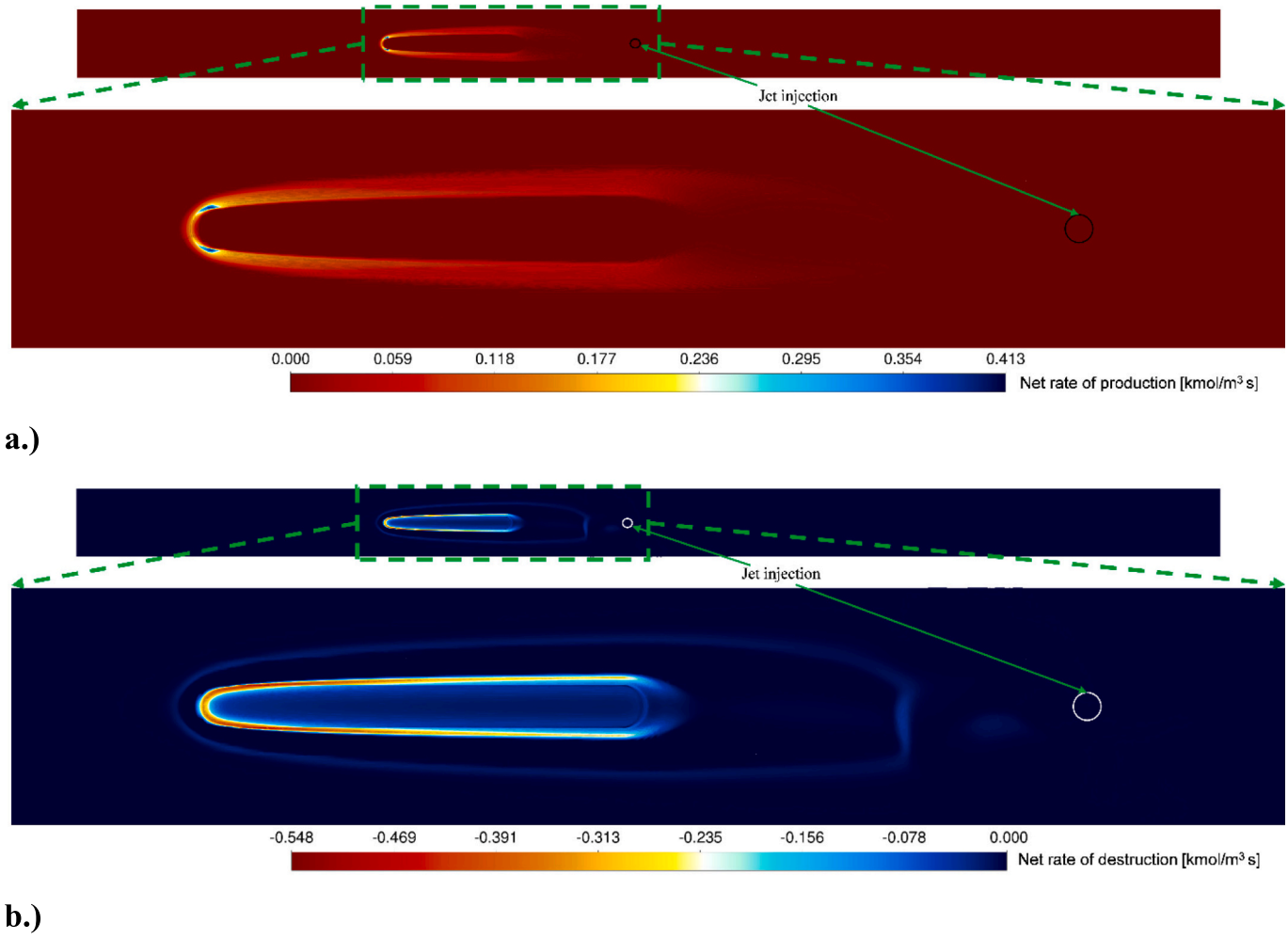

Fig. 10. Regions of a.) net NO formation, and b.) net NO destruction in the reactor.

significant NO loss occurring both upstream and downstream, forming a pronounced downstream tail of negative net NO reactions. By contrast, the introduction of forced jet quenching substantially reduces these destructive zones, steepening local temperature gradients and thereby sustaining the high amount of NO. This demonstrates that forced quenching mitigates backward reactions by stabilizing the NO, leading to a higher overall yield at the reactor outlet, as quantitatively confirmed by Figs. 9–11, which show a reduced spatial extent of net NO destruction in the jet-quenched configuration.

The quenching jets are introduced perpendicular to the reactor centreline, with jet velocities reaching nearly 20 times the velocity of the main inlets. This strong momentum input generates highly turbulent mixing inside the reactor, significantly altering the local fluid dynamics. The jets penetrate deeply into the chemically active zone, directly interacting with the reaction region and reducing the dominance of negative net NO formation. Fig. 12 presents instantaneous streamlines demonstrating jet penetration into the negative net NO region, with isocontour values consistent with those of the net rate of NO destruction shown in Fig. 11. The flow near the jet impingement zone is highly transient and characterized by strong fluctuations in velocity, temperature and species, which can cause rapid local variations in the reaction zone. Nevertheless, the overall stabilizing influence of forced jet quenching remains robust, consistently suppressing NO destruction and sustaining higher net production compared to the non-quenched configuration.

A quantitative comparison between the non-quenched and jet-quenched systems is performed by evaluating the surface integral of the product of velocity component in the x-direction and NO concentration at various positions within the reactor, as shown in Fig. 13.

This analysis, averaged over 10-time steps, provides a direct measure of the effectiveness of forced jet quenching in stabilizing NO yield against thermal destruction. Two non-quenched configurations were considered, corresponding to single main inlet flow rates of 20 SLM and 10 SLM, and compared against a jet-quenched system with a split inlet of 10 + 10 SLM. Fig. 13a indicates that, despite differences in flow configuration, all systems initially follow a similar trajectory: the NO kmole/s increases sharply axially and reaches a peak value, which shows the potential reactor performance, but this would require achieving maximum quenching efficiency. The forced quenching efficiency, $E_Q \in [0,1]$, defined in Eq. (14), measures how effectively forced quenching closes the gap between the maximum NO molar flow rate achievable inside the reactor and the outlet NO molar flow rate obtained under intrinsic quenching conditions. It therefore quantifies the suppression of back-reactions achieved by jet quenching in the reactor.

$$E_Q = \frac{\Phi_{NO,out}^{forced} - \Phi_{NO,out}^{intrinsic}}{\Phi_{NO,peak}^{intrinsic} - \Phi_{NO,out}^{intrinsic}} \tag{14}$$

where $\Phi_{NO}(x)$ is the net NO molar flow rate through a cross-section at axial position x, defined by

$$\Phi_{NO}(x) = \iint c_{NO}(\boldsymbol{u}\cdot\boldsymbol{n})dA \tag{15}$$

where $\boldsymbol{n}$ is the outward unit normal to the cross-section and $\boldsymbol{u}\cdot\boldsymbol{n}$ repre-

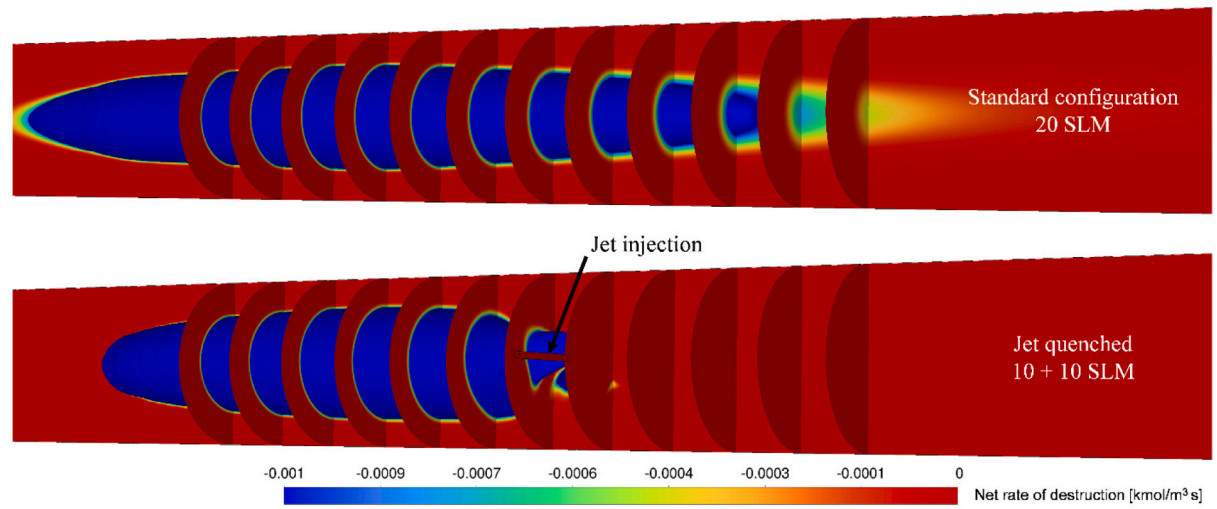

a.)

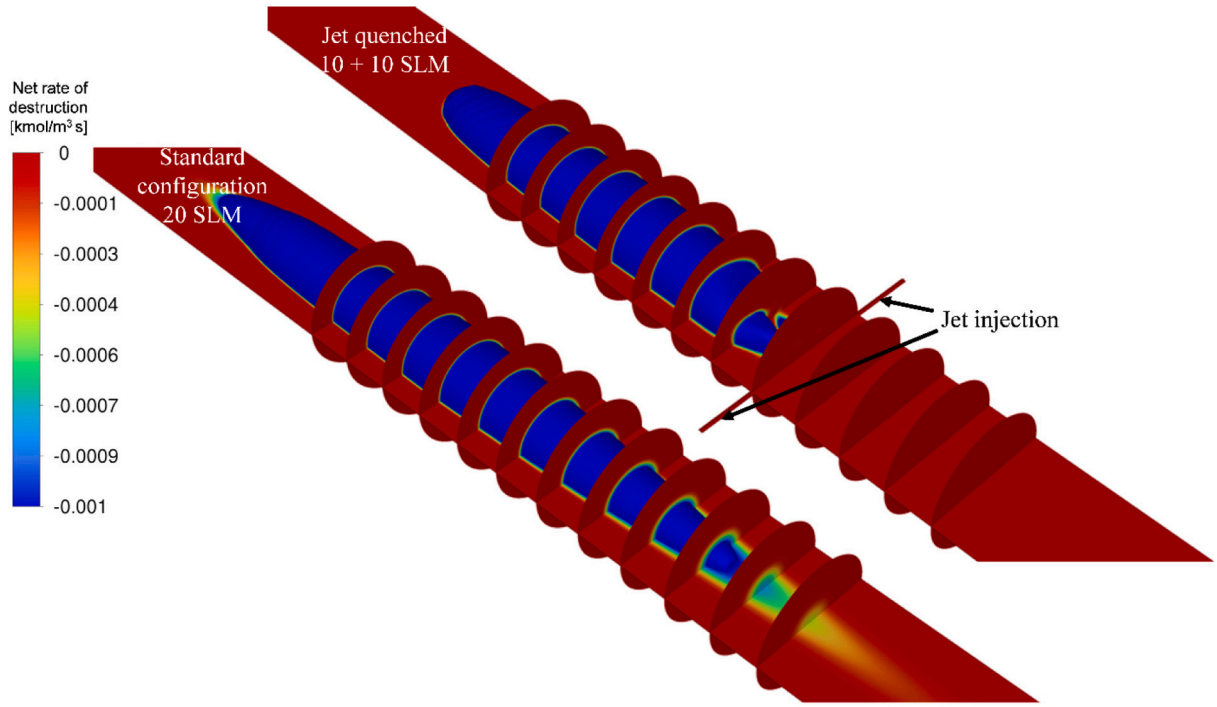

b.)

Fig. 11. Effect of jet quenching on net NO destruction: isocontour (iso value = −0.001) superimposed with contours of net NO destruction in twelve cross-sectional planes throughout the reactor, a.) front view, and b.) isometric view.

sents the local convective flux through the cross section.

In general, the jet-quenched system maintains significantly higher NO levels toward the outlet, as forced cooling suppresses NO destruction as shown in Fig. 13a. It is also clear that the net NO formation profiles for the two cases overlap closely inside the region $0 < x/D < 6$, indicating that the overall NOx formation/destruction upstream is not influenced. Quantitatively, the jet-quenched system achieves a 54.3% quenching efficiency, corresponding to a relative increase in NO yield of 5.7% compared to the non-quenched 20 SLM configuration under identical pressure and power conditions. The shortfall in efficiency, is attributed to limitations of the current jet-injection configuration.

A comparison with the non-quenched 10 SLM configuration, shown

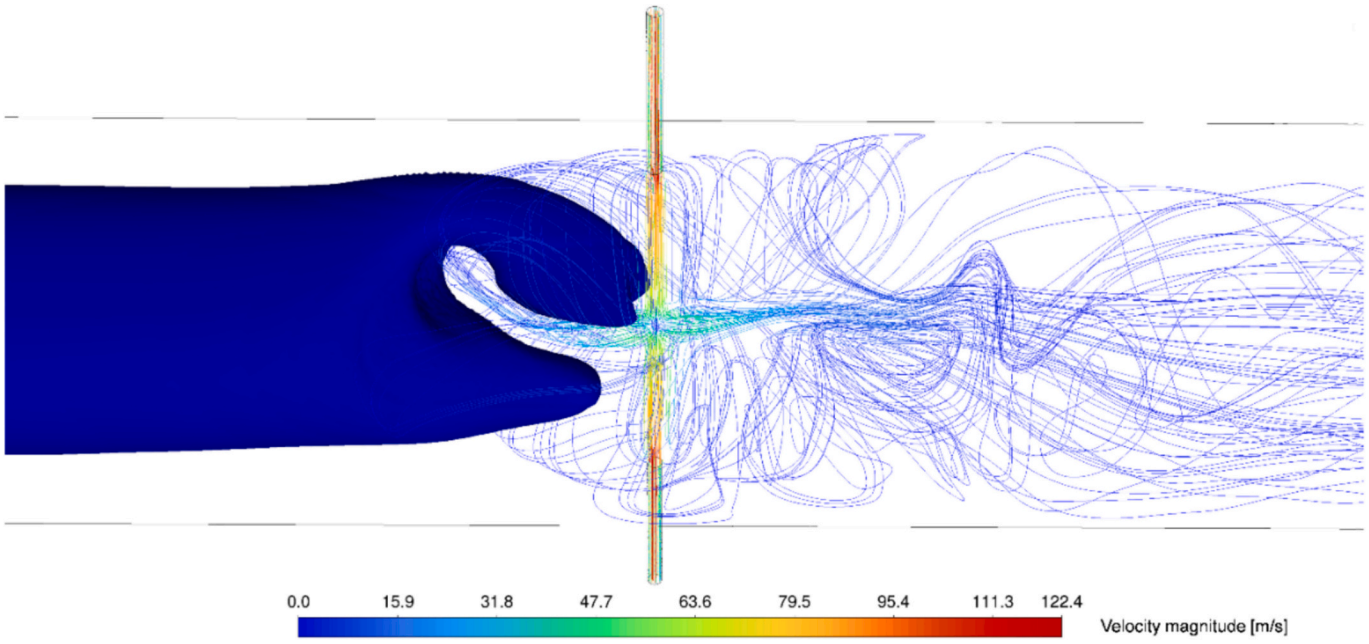

Fig. 12. Jet penetration into the reaction zone, shown by the isocontour of net NO destruction (iso value = −0.001) and velocity streamlines at an instantaneous time.

in Fig. 13b, highlights an even greater relative benefit of forced quenching. Here, the jet-quenched case achieves nearly 70% quenching efficiency, corresponding to a relative increase in NO yield of 9.8% at the outlet, underscoring the importance of active quenching in suppressing backward reactions. These results clearly demonstrate that intrinsic quenching is insufficient to preserve NO at high yields, whereas forced jet quenching provides a robust mechanism for stabilizing NO.

The CFD simulations further confirm that the present model reliably captures the coupled flow dynamics, scalar transport, and chemical kinetics governing NO evolution within the plasma reactor. Fig. 14 presents a parametric assessment of jet injection location. The results reveal that the injection directly adjacent to the core reaction zone (dashed green line) leads to incomplete quenching, as the injected cold gas interferes prematurely, yielding lower overall NO mole fraction at the reactor outlet. Conversely, injection too far downstream produces negligible improvement, since most of the backward reactions have already occurred before quenching is introduced. Thus, the simulations reveal how jet placement influences quenching effectiveness. The present study identifies a jet-injection configuration that is highly effective under the tested operating conditions. We emphasize that this configuration is not claimed to be globally optimal, as only a limited set of injection locations was examined. Preliminary tests indicate that low jet momentum ratios are ineffective, since weak jets are convected downstream and do not penetrate the high-temperature core region, resulting in negligible additional quenching. Other design parameters such as injection angle and number of jets may further influence quenching performance and energy cost and are therefore identified as important directions for future optimization studies. While injection angle was not explored here, angled injection may be viable provided it does not prematurely perturb the plasma core or destabilize the discharge.

Collectively, these findings establish that the addition of forced jet quenching is a more effective strategy than intrinsic quenching alone for achieving high NO yields. They also highlight that further refinement of the quenching strategy-particularly in terms of jet geometry, positioning, and momentum ratios-can lead to significant improvements in plasma reactor performance.

In general, the effectiveness of forced quenching is inherently condition-dependent, as it is governed by the competition between (i) the chemical time scales for NO formation and destruction and (ii) the cooling/mixing time scale imposed by the quenching jet. Quenching is most beneficial when it rapidly reduces temperature after NO has formed in the hot zone, thereby limiting subsequent back-reactions during cooling. While the magnitude of the effect depends on operating conditions such as power, pressure, and gas temperature, the same quenching concept can be applied to other regimes where intrinsic quenching alone is insufficient.

5. Conclusions

This study comprehensively investigates the role of forced jet quenching in enhancing nitrogen fixation efficiency within a microwave plasma reactor using three-dimensional transient simulations of reactive turbulent flow. The introduction of high-momentum jets fundamentally restructures the internal fluid dynamics, generating intense turbulence, localized recirculation, and strong mixing that synergistically interact with the swirl induced by tangential inlets. These effects not only accelerate the redistribution of momentum but also establish steep radial and axial temperature gradients critical for effective quenching. Temperature field analysis demonstrates that quenching jets rapidly reduce plasma tail region from ~3500 K to below 800 K within the interaction zone, while maintaining low wall temperatures. This abrupt cooling suppresses radical mediated backward reactions, effectively freezing the gas composition and limiting further losses by preventing continued re-equilibration during rapid cooling from high temperature. The simulations further reveal that intrinsic quenching, although effective radially, is insufficient to prevent extensive NO destruction in the downstream region. There, the gas remains at high temperature, and NO can continue to decompose unless it is cooled. In contrast, forced jet quenching significantly reduces destructive zones, sustaining a higher net NO yield toward the reactor outlet. Quantitative comparisons with non-quenched configurations demonstrate the substantial benefit of jet-assisted quenching. At 400 W, forced quenching suppresses back-reactions and increases the outlet NO yield by 5.7% relative to the 20 SLM intrinsic-quenching case and by 9.8% relative to the 10 SLM case, both values increasing further at higher power. These gains are achieved without compromising energy efficiency, as evidenced by lower specific energy costs and strong agreement between CFD predictions and experimental measurements across a wide range of operating power

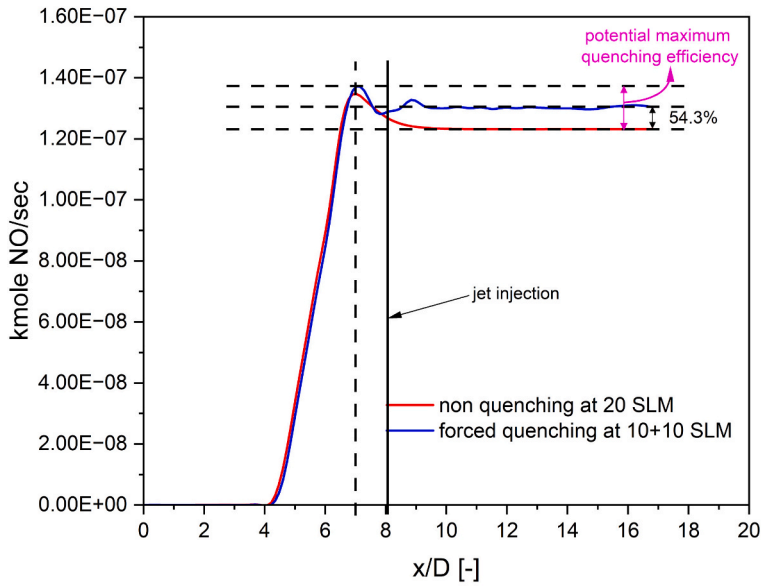

a.)

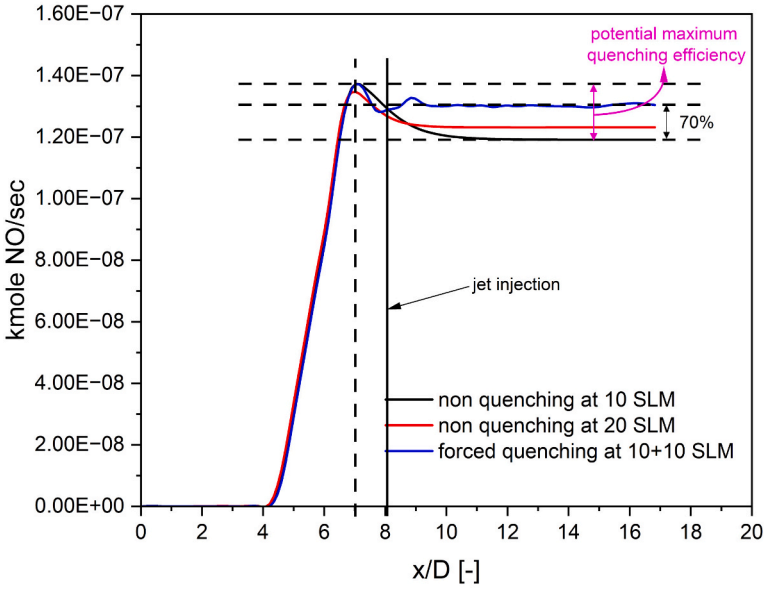

b.)

Fig. 13. Comparison of non-quenched and jet quenched reactor systems at different operating conditions: a.) with and without forced jet quenching, b.), different flow rates.

inputs. Experimentally, the specific energy consumption decreased by approximately 14–17% for the quenched configuration relative to the non-quenched case, while the CFD simulations predicted a corresponding reduction of 6–8%. Furthermore, parametric analysis of jet placement highlights the effect of quenching location: jets introduced too close to the reactor core interfere and reduce NO formation, while jets positioned too far downstream offer limited benefit. From a design perspective, the results suggest that higher NO_x yield and lower energy cost can be achieved by injecting the quench flow at the onset of the net NO-destruction zone and by tuning jet penetration strength to maximize cooling while avoiding interference with the formation zone. These insights emphasize that the efficiency of plasma-based nitrogen fixation can be further enhanced through optimized jet configuration and injection strategy. Overall, this work demonstrates that forced jet quenching provides stable operation despite large fluid dynamics disturbances from the impinging jets. In particular, forced quenching acts as a robust, controllable complement that augments the reactor's intrinsic quenching, by (i) suppressing downstream NO destruction, (ii) providing a systematic increase in yield, and (iii) measurably reducing the specific energy cost. The reported improvements are valid for the present configurations and the explored power and pressure ranges. Likewise, the findings of the present study suggest that the attainable performance limit is close to the results achieved.

CRediT authorship contribution statement

Vikash Vashisth: Writing – review & editing, Writing – original draft, Visualization, Validation, Software, Investigation, Formal analysis. **Muzammil Iqbal:** Writing – review & editing, Methodology, Investigation, Data curation. **Thomas Butterworth:** Writing – review & editing, Writing – original draft, Supervision, Resources, Methodology, Investigation, Formal analysis. **Gerard van Rooij:** Writing – review &

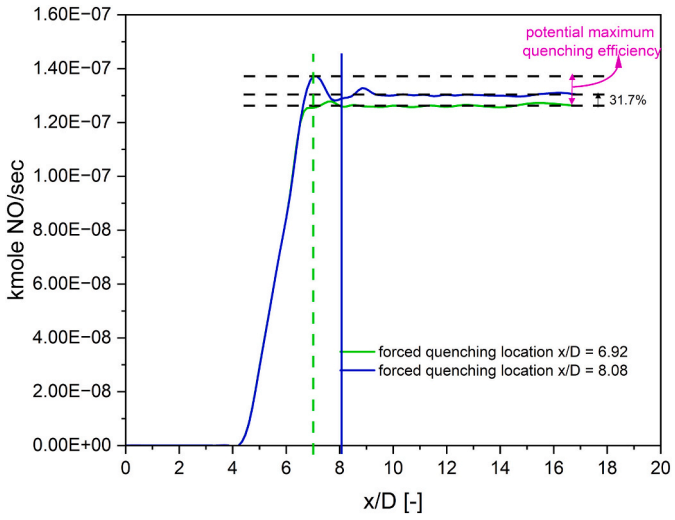

Fig. 14. Effect of jet injection location within the reactor on nitrogen fixation.

editing, Supervision, Project administration, Investigation, Funding acquisition. **Ronnie Andersson:** Writing – review & editing, Writing – original draft, Supervision, Project administration, Methodology, Funding acquisition, Formal analysis, Conceptualization.

Declaration of competing interest

The authors declare that they have no known competing financial interests or personal relationships that could have appeared to influence the work reported in this paper.

Acknowledgments

Financial support from the Swedish Board of Agriculture (Grant: 2021-3998-4) is gratefully acknowledged. The computations were enabled by resources provided by the National Academic Infrastructure for Supercomputing in Sweden (NAISS) at Chalmers e-Commons/C3SE partially funded by the Swedish Research Council through grant agreement no. 2022-06725.

Appendix A. Supplementary data

Supplementary data to this article can be found online at https://doi.org/10.1016/j.cej.2026.178575.

Data availability

Data will be made available on request.

References

[1] N. Cherkasov, A.O. Ibhadon, P. Fitzpatrick, A review of the existing and alternative methods for greener nitrogen fixation, Chem. Eng. Process. Process Intensif. 90 (2015) 24–33, https://doi.org/10.1016/j.cep.2015.02.004.
[2] B.S. Patil, Q. Wang, V. Hessel, J. Lang, Plasma N2-fixation: 1900–2014, Catal. Today 256 (2015) 49–66, https://doi.org/10.1016/j.cattod.2015.05.005.
[3] J.L. Liu, L.L. Nie, D.W. Liu, X.P. Lu, Plasma for nitrogen fixation by using N2/O2 mixture: reaction pathway, energy flow, and plasma reactor, Plasma Process. Polym. 21 (2024), https://doi.org/10.1002/ppap.202300153.
[4] K.H.R. Rouwenhorst, F. Jardali, A. Bogaerts, L. Lefferts, From the Birkeland-Eyde process towards energy-efficient plasma-based NOx synthesis: a techno-economic analysis, Energy Environ. Sci. 14 (2021) 2520–2534, https://doi.org/10.1039/d0ee03763j.
[5] A.A. Abdelaziz, A. Komuro, Y. Teramoto, M. Schiorlin, D.Y. Kim, T. Nozaki, H. H. Kim, Atmospheric-pressure plasmas for NOx production: short review on current status, Curr. Opin. Green Sustain. Chem. 50 (2024) 100977, https://doi.org/10.1016/j.cogsc.2024.100977.
[6] X. Pei, D. Gidon, Y.J. Yang, Z. Xiong, D.B. Graves, Reducing energy cost of NOx production in air plasmas, Chem. Eng. J. 362 (2019) 217–228, https://doi.org/10.1016/j.cej.2019.01.011.
[7] X. Pei, D. Gidon, D.B. Graves, Specific energy cost for nitrogen fixation as NOxusing DC glow discharge in air, J. Phys. D Appl. Phys. 53 (2020), https://doi.org/10.1088/1361-6463/ab5095.
[8] P. Lamichhane, N. Pourali, E.V. Rebrov, V. Hessel, Energy intensified nitrogen fixation through fast modulated gas discharge from pyramid-shaped micro-electrode, Plasma Chem. Plasma Process. 44 (2024) 1369–1392, https://doi.org/10.1007/s11090-023-10376-1.
[9] S. Van Alphen, H. Ahmadi Eshtehardi, C. O'Modhrain, J. Bogaerts, H. Van Poyer, J. Creel, M.P. Delplancke, R. Snyders, A. Bogaerts, Effusion nozzle for energy-efficient NOx production in a rotating gliding arc plasma reactor, Chem. Eng. J. 443 (2022) 136529, https://doi.org/10.1016/j.cej.2022.136529.
[10] W. Wang, D. Mei, X. Tu, A. Bogaerts, Gliding arc plasma for CO2 conversion: better insights by a combined experimental and modelling approach, Chem. Eng. J. 330 (2017) 11–25, https://doi.org/10.1016/j.cej.2017.07.133.
[11] S. Li, J.A. Medrano, V. Hessel, F. Gallucci, Recent progress of plasma-assisted nitrogen fixation research: a review, Processes 6 (2018), https://doi.org/10.3390/pr6120248.
[12] S. Kelly, A. Bogaerts, Nitrogen fixation in an electrode-free microwave plasma, Joule 5 (2021) 3006–3030, https://doi.org/10.1016/j.joule.2021.09.009.
[13] V. Hessel, G. Cravotto, P. Fitzpatrick, B.S. Patil, J. Lang, W. Bonrath, Industrial applications of plasma, microwave and ultrasound techniques: nitrogen-fixation and hydrogenation reactions, Chem. Eng. Process. Process Intensif. 71 (2013) 19–30, https://doi.org/10.1016/j.cep.2013.02.002.
[14] S. Kelly, C. Verheyen, A. Cowley, A. Bogaerts, Producing oxygen and fertilizer with the Martian atmosphere by using microwave plasma, Chem 8 (2022) 2797–2816, https://doi.org/10.1016/j.chempr.2022.07.015.
[15] Q. Shen, A. Pikalev, J. Gans, L. Kuijpers, A. Hughes, V. Guerra, M.C.M. van de Sanden, Boosting the NOx production in microwave air plasma: a synergy of chemistry and vibrational kinetics, Plasma Sources Sci. Technol. 35 (2026) 015013, https://doi.org/10.1088/1361-6595/ae2d91.
[16] S. Helsloot, O. Samadi, M. Iqbal, G. van Rooij, T. Butterworth, Trace methane destruction within the effluent of microwave plasma, ACS Omega 10 (2025) 26392–26402, https://doi.org/10.1021/acsomega.4c10550.
[17] H.M.S. Van Poyer, I. Tsonev, S.J.R. Maerivoet, M.C.K. Albrechts, A. Bogaerts, Influence of radial transport and turbulent effects on CO2 conversion in a microwave plasma reactor: insights from a multi-dimensional thermo-chemical flow model, Chem. Eng. J. 507 (2025) 160688, https://doi.org/10.1016/j.cej.2025.160688.
[18] J. Lee, H. Sun, S.K. Im, M. Soo Bak, Formation of nitrogen oxides from atmospheric electrodeless microwave plasmas in nitrogen-oxygen mixtures, J. Appl. Phys. 122 (2017), https://doi.org/10.1063/1.4996790.
[19] S. Wu, Y. Liao, K. Feng, F. Zheng, W. Xiao, Nitrogen fixation by atmospheric microwave plasma with local electric field enhancement, J. Phys. D Appl. Phys. 58 (2025), https://doi.org/10.1088/1361-6463/ad7d16.
[20] F. Zheng, K. Feng, S. Wu, W. Xiao, Experimental investigation into atmospheric microwave plasma-driven nitrogen fixation using metal–organic frameworks, Processes 12 (2024), https://doi.org/10.3390/pr12122633.
[21] K. Feng, S. Wu, F. Zheng, W. Xiao, A novel atmospheric microwave plasma source based on circular waveguide with double ridges for nitrogen fixation, Phys. Scr. 100 (2025), https://doi.org/10.1088/1402-4896/ad96ef.
[22] R. Snoeckx, A. Bogaerts, Plasma technology-a novel solution for CO2 conversion? Chem. Soc. Rev. 46 (2017) 5805–5863, https://doi.org/10.1039/c6cs00066e.
[23] C.K. Kiefer, R. Antunes, A. Hecimovic, A. Meindl, U. Fantz, CO2 dissociation using a lab-scale microwave plasma torch: an experimental study in view of industrial application, Chem. Eng. J. 481 (2024), https://doi.org/10.1016/j.cej.2023.148326.
[24] R. Rincón, A. Marinas, J. Muñoz, C. Melero, M.D. Calzada, Experimental research on ethanol-chemistry decomposition routes in a microwave plasma torch for hydrogen production, Chem. Eng. J. 284 (2016) 1117–1126, https://doi.org/10.1016/j.cej.2015.09.062.
[25] N. Kaushik, S. Mitra, E.J. Baek, L.N. Nguyen, P. Bhartiya, J.H. Kim, E.H. Choi, N. K. Kaushik, The inactivation and destruction of viruses by reactive oxygen species generated through physical and cold atmospheric plasma techniques: current status and perspectives, J. Adv. Res. 43 (2023) 59–71, https://doi.org/10.1016/j.jare.2022.03.002.
[26] P. Shaw, N. Kumar, H.S. Kwak, J.H. Park, H.S. Uhm, A. Bogaerts, E.H. Choi, P. Attri, Bacterial inactivation by plasma treated water enhanced by reactive nitrogen species, Sci. Rep. 8 (2018) 1–10, https://doi.org/10.1038/s41598-018-29549-6.
[27] N.K. Kaushik, P. Bhartiya, N. Kaushik, Y. Shin, L.N. Nguyen, J.S. Park, D. Kim, E. H. Choi, Nitric-oxide enriched plasma-activated water inactivates 229E coronavirus and alters antiviral response genes in human lung host cells, Bioact. Mater. 19 (2023) 569–580, https://doi.org/10.1016/j.bioactmat.2022.05.005.
[28] R. Quiroz Marnef, S. Maerivoet, I. Tsonev, F. Reniers, A. Bogaerts, Spatially resolved modelling of NH3 cracking in warm plasma, Chem. Eng. J. 508 (2025), https://doi.org/10.1016/j.cej.2025.161180.
[29] S. Wang, V. Rohani, P. Dupont, S. Pagnon, L. Fulcheri, A chemical kinetics simulation of plasma-catalytic dry reforming, Chem. Phys. 574 (2023) 112017, https://doi.org/10.1016/j.chemphys.2023.112017.
[30] M. Tatar, V. Vashisth, M. Iqbal, T. Butterworth, G. van Rooij, R. Andersson, Analysis of a plasma reactor performance for direct nitrogen fixation by use of three-dimensional simulations and experiments, Chem. Eng. J. 497 (2024) 154756, https://doi.org/10.1016/j.cej.2024.154756.

[31] J. Perambadur, A.Y. Klimenko, V. Rudolph, P. Shukla, Investigation of plasma swirl dynamics and effects of secondary gas injection in a vortex gas stabilized DC arc plasma, Int. J. Heat Fluid Flow 95 (2022) 108978, https://doi.org/10.1016/j.ijheatfluidflow.2022.108978.
[32] M. Majeed, M. Iqbal, M. Altin, Y.N. Kim, D.K. Dinh, C. Lee, Z. Ali, D.H. Lee, Effect of thermal gas quenching on NOx production by atmospheric pressure rotating arc plasma: a pathway towards eco-friendly fertilizer, Chem. Eng. J. 485 (2024) 149727, https://doi.org/10.1016/j.cej.2024.149727.
[33] S. Van Alphen, A. Hecimovic, C.K. Kiefer, U. Fantz, R. Snyders, A. Bogaerts, Modelling post-plasma quenching nozzles for improving the performance of CO2 microwave plasmas, Chem. Eng. J. 462 (2023) 142217, https://doi.org/10.1016/j.cej.2023.142217.
[34] C. Park, Review of chemical-kinetic problems of future NASA missions. I - earth entries, J. Thermophys. Heat Transf. 7 (1993) 385–398, https://doi.org/10.2514/3.431.
[35] A.W. van de Steeg, T. Butterworth, D.C.M. van den Bekerom, A.F. Silva, M.C. M. van de Sanden, G.J. van Rooij, Plasma activation of N2, CH4 and CO2: an assessment of the vibrational non-equilibrium time window, Plasma Sources Sci. Technol. 29 (2020), https://doi.org/10.1088/1361-6595/abbae4.
[36] R.B. Bird, W.E. Stewart, E.N. Lightfoot, R.E. Meredith, Transport phenomena, J. Electrochem. Soc. 108 (1961) 78C, https://doi.org/10.1149/1.2428074.
[37] Stephen B. Pope, Turbulent flows, Meas. Sci. Technol. 12 (2001) 2020, https://doi.org/10.1088/0957-0233/12/11/705.
[38] S.B. Pope, Ten questions concerning the large-eddy simulation of turbulent flows, New J. Phys. 6 (2004), https://doi.org/10.1088/1367-2630/6/1/035.
[39] B. Andersson, R. Andersson, L. Håkansson, M. Mortensen, R. Sudiyo, B. van Wachem, Computational Fluid Dynamics for Engineers, Cambridge University Press, Cambridge, 2011, https://doi.org/10.1017/CBO9781139093590.